

## Defected vanadium bronzes as superb cathodes in aqueous zinc-ion batteries

Jianwei Li<sup>1</sup>, Ningjing Luo<sup>2</sup>, Feng Wan<sup>1</sup>, Siyu Zhao<sup>1</sup>, Zhuangnan Li<sup>1</sup>, Wenyao Li<sup>1,3,5</sup>, Jian Guo<sup>1</sup>, Paul R. Shearing<sup>3</sup>, Dan J.L. Brett<sup>3</sup>, Claire J. Carmalt<sup>1</sup>, Guoliang Chai<sup>2\*</sup>, Guanjie He<sup>1,3,4\*</sup> and Ivan P. Parkin<sup>1\*</sup>

<sup>1</sup>Christopher Ingold Laboratory, Department of Chemistry, University College London, 20 Gordon Street, London WC1H 0AJ, U.K. Email: g.he@ucl.ac.uk; i.p.parkin@ucl.ac.uk

<sup>2</sup>State Key Laboratory of Structural Chemistry, Fujian Institute of Research on the Structure of Matter, Chinese Academy of Sciences (CAS), Fuzhou, 350002 Fujian, P.R. China. Email: g.chai@fjirsm.ac.cn

<sup>3</sup>Electrochemical Innovation Lab, Department of Chemical Engineering, University College London, London WC1E 7JE, U.K.

<sup>4</sup>School of Chemistry, University of Lincoln, Joseph Banks Laboratories, Green Lane, Lincoln, LN6 7DL, U.K.

<sup>5</sup>School of Materials Engineering, Shanghai University of Engineering Science, Shanghai 201620, China.

### 1. Experimental section

**Synthesis:** NVO and O<sub>d</sub>-NVO were both prepared by the single-step hydrothermal reaction but with a slight variation on the amount of precursors used. In a typical synthesis of NVO, 5 mmol of ammonium metavanadate was dissolved into 30 mL of deionized water with 10 min stirring under ambient environment. After that, 2 mmol of oxalic acid was added into the previous solution with additional 30 min magnetic stirring, while, a mixture of 6 mmol of oxalic acid and 1 mmol of ammonium fluoride were added for the preparation of O<sub>d</sub>-NVO, instead. Both of the resulting solutions were transferred into 50 mL Teflon-lined autoclaves, respectively, and heat up to 180 °C for 6 hours. Then, the as-obtained bronze-color precipitates were washed by deionized water several times and finally collected by centrifuge. All washed samples were freeze-dried for 2 days.

**Characterizations:** FT-IR data were attained by Attenuated Total Reflectance Fourier transform infrared spectroscopy (ATRFTIR, BRUKER, platinum-ATR). All X-ray diffraction (XRD) patterns were characterized by a STOE SEIFERT diffractometer *via* Mo K $\alpha$  radiation source ( $\lambda = 0.7093 \text{ \AA}$ ). The detected angular was chosen from  $2^\circ < 2\theta < 45^\circ$ . Additionally, the morphology and microstructure images of the as-obtained samples were observed by scanning electron microscopy (SEM, Carl Zeiss EVO MA10) and transmission electron microscopy (TEM JEOL, JEM-2100), respectively. The chemical states and elemental analysis were achieved by X-ray photoelectron spectroscopy (XPS, Thermo scientific K-alpha photoelectron spectrometer with an Al source). Casa XPS was adopted for the analysis of XPS results with the calibration of adventitious carbon at the binding energy of 284.8 eV.

**Electrochemical evaluation:** 2-electrode testing protocols were achieved by CR2032 coin cells for battery performance measurements. Additionally, Swagelok cells were adopted for all CV, EIS and *ex-situ* characterizations. The cathode electrodes were fabricated by mixing polyvinylidene fluoride (Sigma-Aldrich), Super-P (Sigma-Aldrich) and as-prepared samples with a ratio of 1:2:7. The mixture slurry was printed on a hydrophilic carbon paper and then transferred to a vacuum oven drying under 70 °C for 12 h. The dried electrode was weighted by an analytical balance (Ohaus;  $\delta = 0.01 \text{ mg}$ ) to calculate the loading mass of active materials (1.5-2.5 mg cm $^{-2}$ ). The anodes of the AZIBs directly utilized zinc metal foil (99.9%) with no further treatments. 3 M Zn(CF $_3$ SO $_3$ ) $_2$  (Sigma-Aldrich) aqueous solution was adopted as the electrolyte, and glass-fiber (GF/A, Whatman) was chosen as separators. The evaluation of CV, EIS and battery performance tests were achieved by a VMP3 Biologic potentiostat and Neware battery testing system.

### Calculation details

Density functional theory (DFT) calculations were performed using the VASP (Vienna ab initio simulation package).<sup>1,2</sup> The generalized gradient approximation (GGA) of Perdew–Burke–Ernzerhof (PBE)<sup>3</sup> was used for the exchange-correlation functional. The projector-augmented-wave (PAW) potentials<sup>4</sup> provided in the VASP package with 2s $^2$ 2p $^3$ , 2s $^2$ 2p $^4$ , 1s $^1$

and  $3p^63d^54s^1$  as the valence-electron configuration were adopted for N, O, H, and V, respectively. The cutoff energy for plane-wave basis sets was set to 520 eV. To eliminate the influence from the periodic boundary condition, the  $1\times3\times1$   $\text{NH}_4\text{V}_4\text{O}_{10}$  supercell was used for the defect calculation of oxygen point vacancies. To incorporate the strong Coulomb repulsion of partly filled valence  $d$  shells of V, the simplified GGA+U method was used with  $U_{\text{eff}}=3.0$  eV ( $J=0$  eV) according to the literature.<sup>5</sup> The optB86-vdW functional, an optimized exchange van der Waals functionals, were applied to incorporate the van der Waals interactions in the systems.<sup>6</sup> All the atoms coordinates were fully relaxed until the magnitude of forces were less than  $0.02$  eV / Å per atom.

To assess the mobility of Zn ions in perfect and defective- $\text{NH}_4\text{V}_4\text{O}_{10}$ , the climbing-image nudged elastic band method (CI-NEB) has also been used to determine the diffusion barriers, and all transition-state structures have been characterized by calculating the vibrational frequencies.<sup>18</sup>

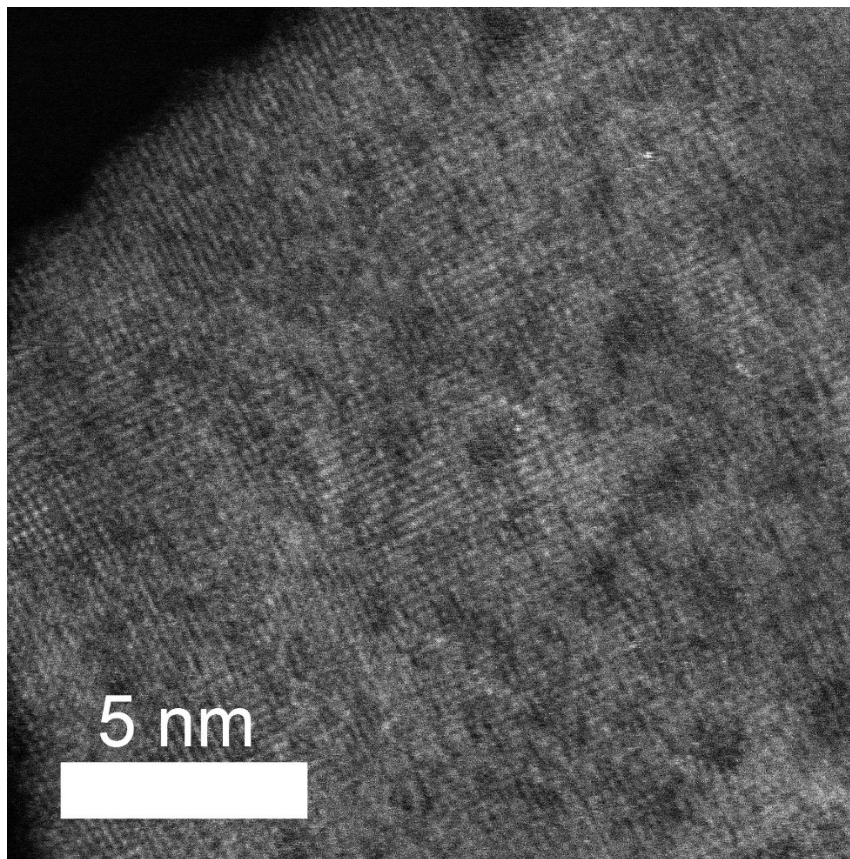


**Figure S1.** High-magnification TEM images of as-obtained  $\text{NH}_4\text{V}_4\text{O}_{10}$  (NVO) materials.

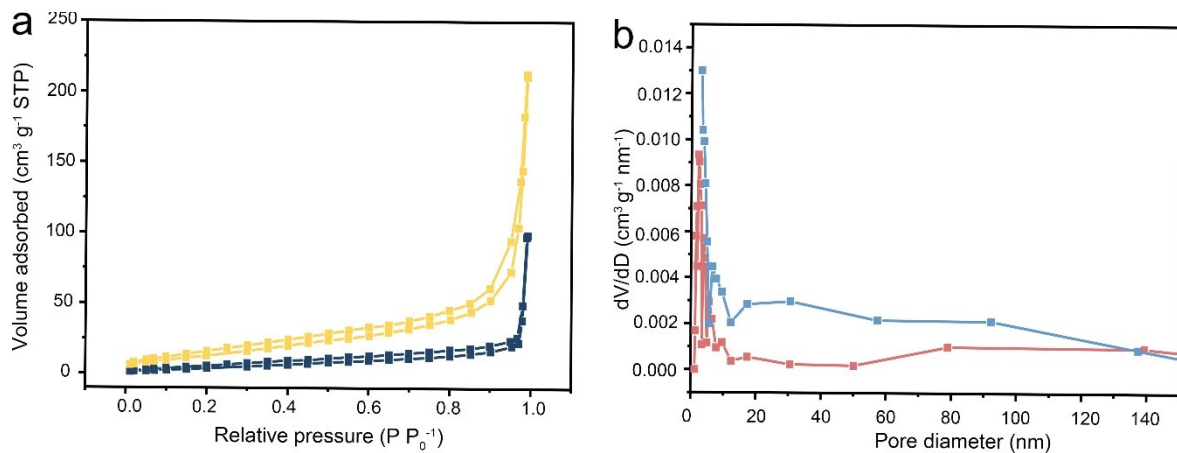


**Figure S2.** a) N<sub>2</sub> adsorption-desorption isotherm, b) and its corresponding pore size distribution.

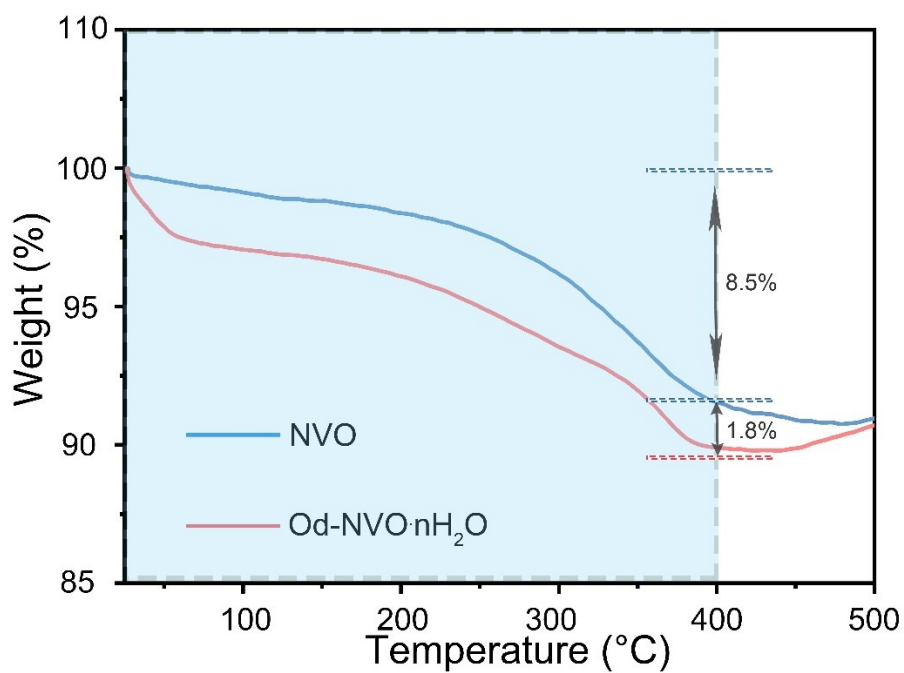


**Figure S3.** TGA results of the NVO and O<sub>d</sub>-NVO·nH<sub>2</sub>O, respectively.

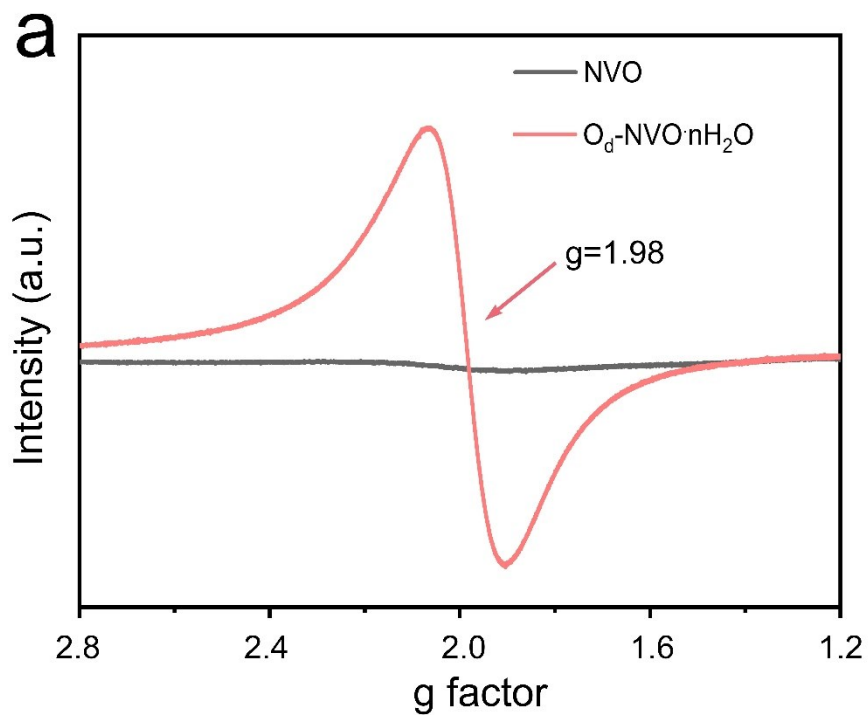


**Figure S4a).** EPR spectra of as-prepared NVO and  $O_d$ -NVO-nH<sub>2</sub>O

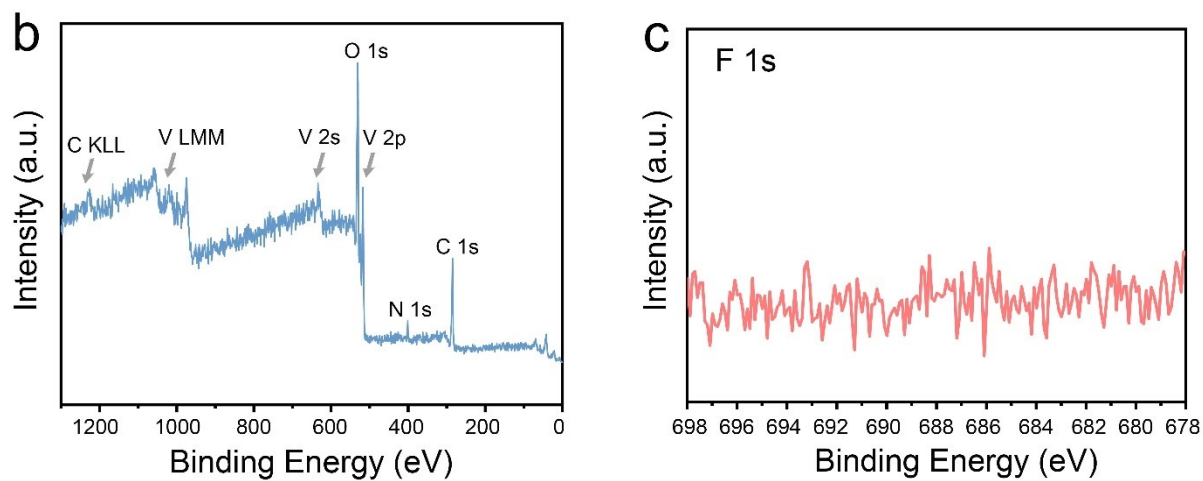


**Figure S4 b)** XPS survey spectrum of pristine  $O_d$ -NVO-nH<sub>2</sub>O and its c) core level spectrum of F 1s.

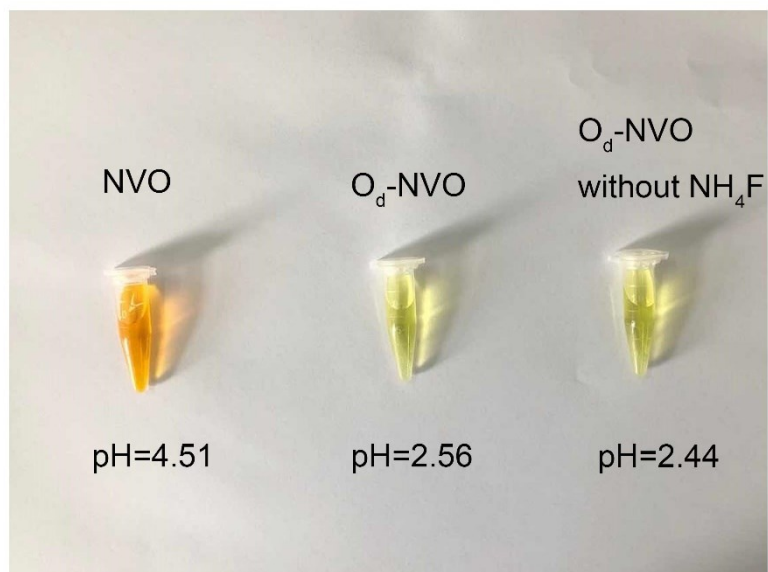


**Figure S5.** pH value of different precursor solution: NVO, O<sub>d</sub>-NVO and O<sub>d</sub>-NVO without NH<sub>4</sub>F, respectively.

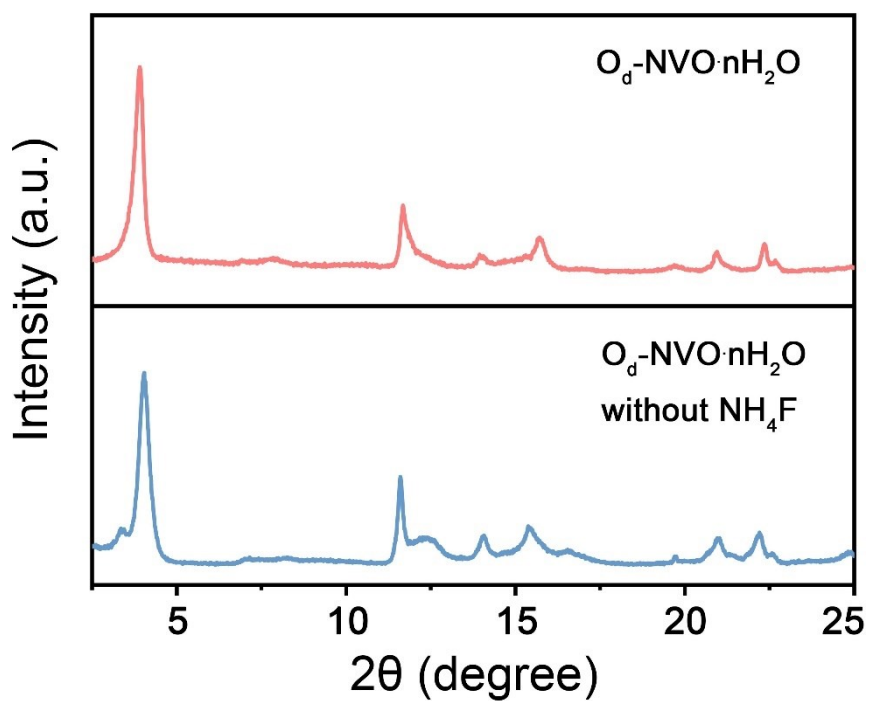


**Figure S6.** XRD patterns of as-prepared O<sub>d</sub>-NVO·nH<sub>2</sub>O and O<sub>d</sub>-NVO·nH<sub>2</sub>O without adding

NH<sub>4</sub>F.

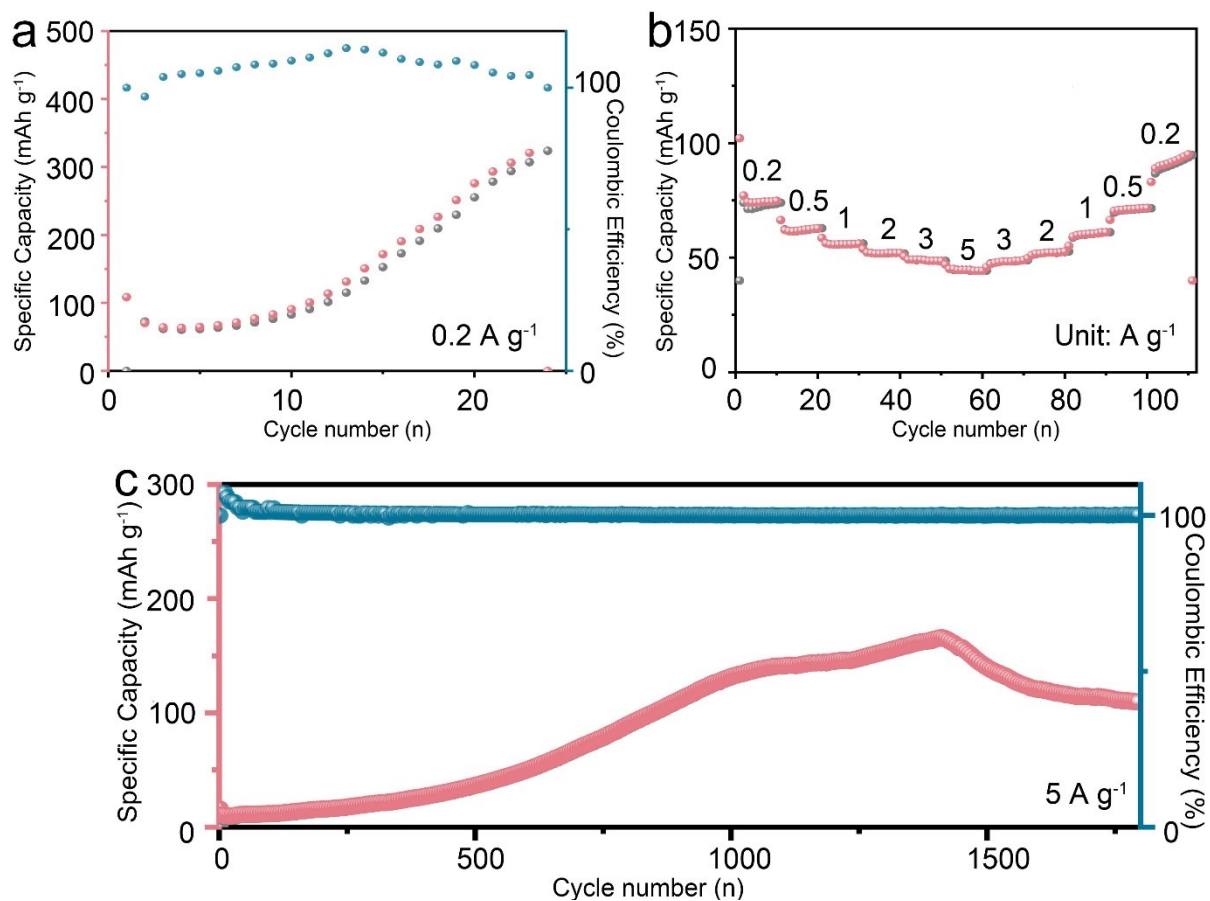


**Figure S7.** Galvanostatic charge/discharge (GCD) profiles for commercial V<sub>2</sub>O<sub>5</sub> cathodes: a) long-cycle measurement at 0.2 A g<sup>-1</sup>; b) rate performance with current density of 0.2, 0.5, 1, 2, 3, 5 A g<sup>-1</sup>, respectively; c) long-cycle measurement of the cells at 5 A g<sup>-1</sup>.

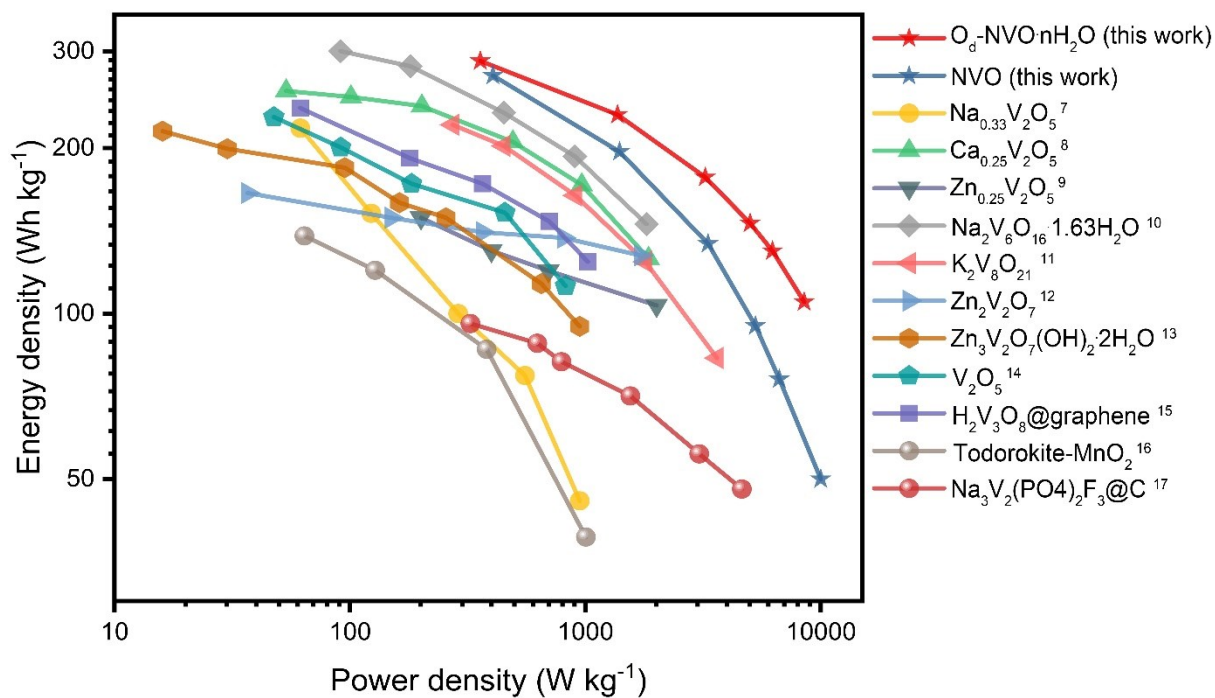


**Figure S8.** Ragone plot of as-developed  $O_d$ -NVO· $nH_2O$ , NVO and other previous reported cathode materials for AZIBs.<sup>7891011121314151617</sup>

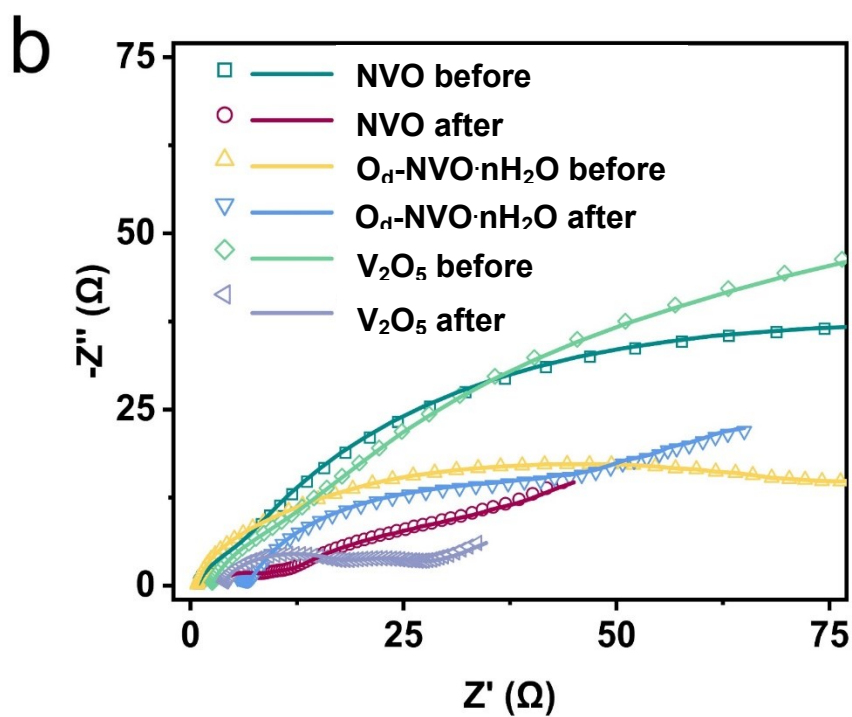
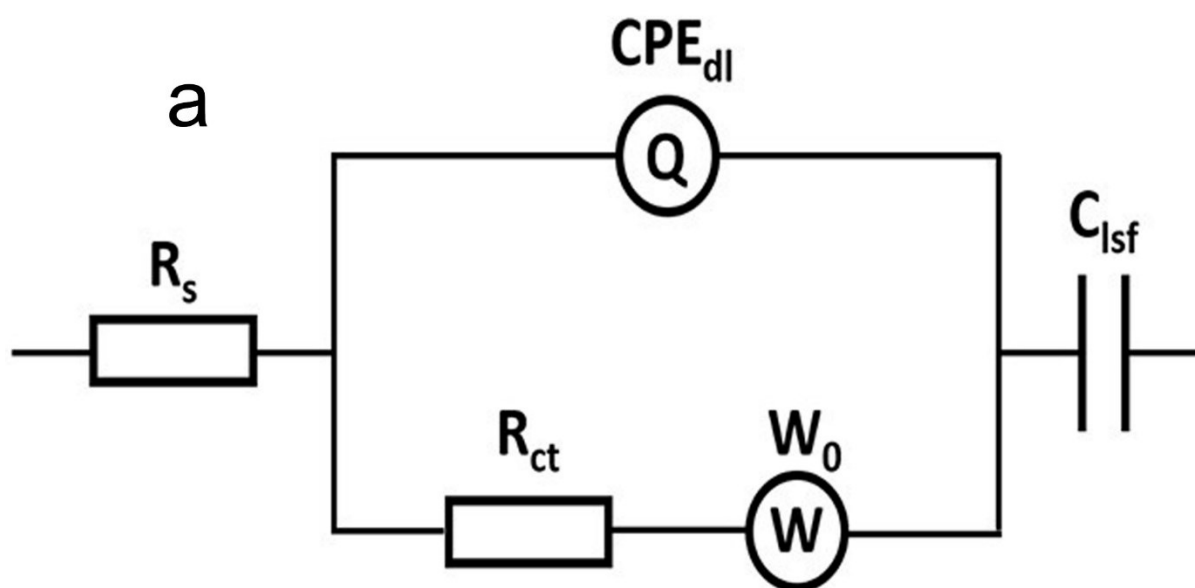


**Figure S9.** a) The equivalent circuit for EIS fitting. b) Electrochemical impedance spectroscopy of NVO, O<sub>d</sub>-NVO·nH<sub>2</sub>O and commercial V<sub>2</sub>O<sub>5</sub> electrodes at initial and after cycles.

**Table S1.** Fitted EIS parametersNB: ( $R_s$ : Combined internal resistance,  $R_{ct}$ : Interfacial charge transfer resistance)

Electrode	$R_s$ ( $\Omega$ )	$R_{ct}$ ( $\Omega$ )
NVO before	0.64	128.8
NVO after	2.78	52.6
O <sub>d</sub> -NVO·nH <sub>2</sub> O before	0.68	33.4
O <sub>d</sub> -NVO·nH <sub>2</sub> O after	2.20	22.5
Commercial V <sub>2</sub> O <sub>5</sub> before	1.93	186.2
Commercial V <sub>2</sub> O <sub>5</sub> after	1.56	33.6

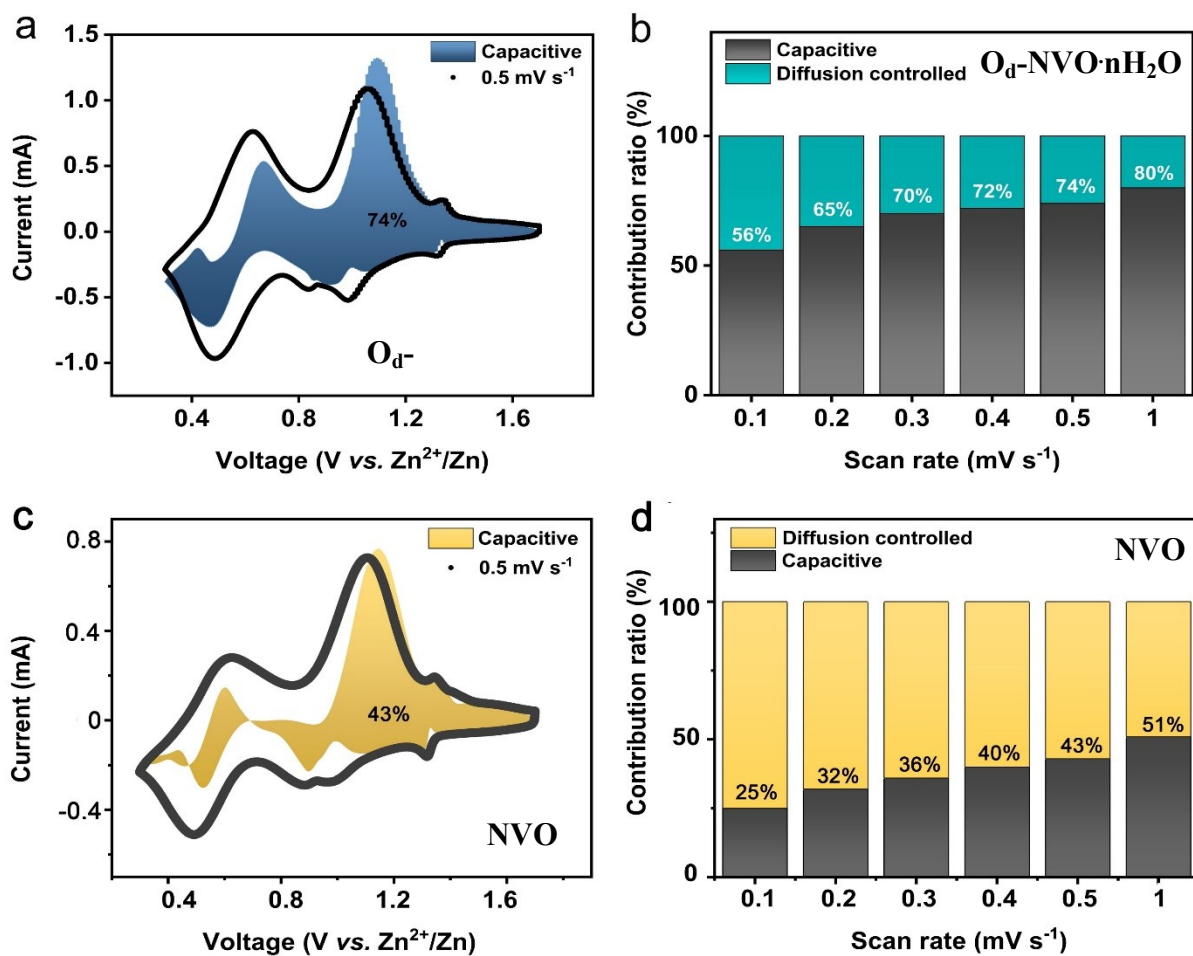


**Figure S10.** a) The CV curve of the  $\text{O}_d^- \text{NVO} \cdot n\text{H}_2\text{O}$  cathode presenting the capacitive contribution (blue region) for total current response at  $0.5 \text{ mV s}^{-1}$ ; b) the contribution ratios of the capacitive and diffusion-controlled reaction behaviors of the as-developed  $\text{O}_d^- \text{NVO} \cdot n\text{H}_2\text{O}$  cathode; c) the CV curve of NVO cathode illustrating the capacitive contribution (yellow region) for total current response at  $0.5 \text{ mV s}^{-1}$ ; d) the contribution ratios of the capacitive and diffusion-controlled reaction behaviors of NVO electrode.

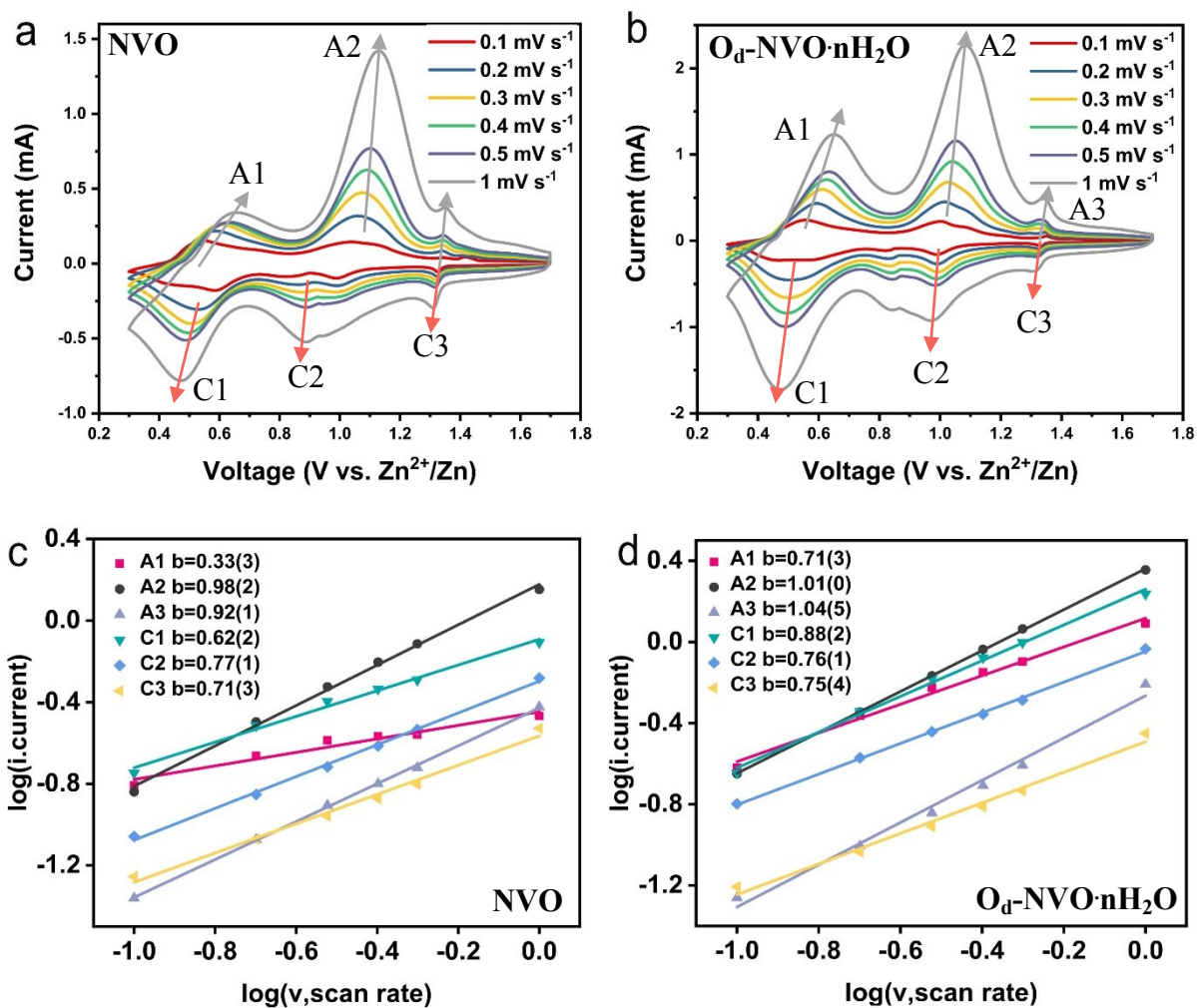


**Figure S11.** a,c) The CV plots of the NVO cells with different sweep rates from  $0.1 \text{ mV s}^{-1}$  to  $1 \text{ mV s}^{-1}$  and its  $b$  value derived from  $\log i$  vs.  $\log v$  plots according to the CV results at selected peaks; b,d) the CV curves of  $O_d$ -NVO· $nH_2O$  with different sweep rates from  $0.1 \text{ mV s}^{-1}$  to  $1 \text{ mV s}^{-1}$  and its corresponding  $b$  value.

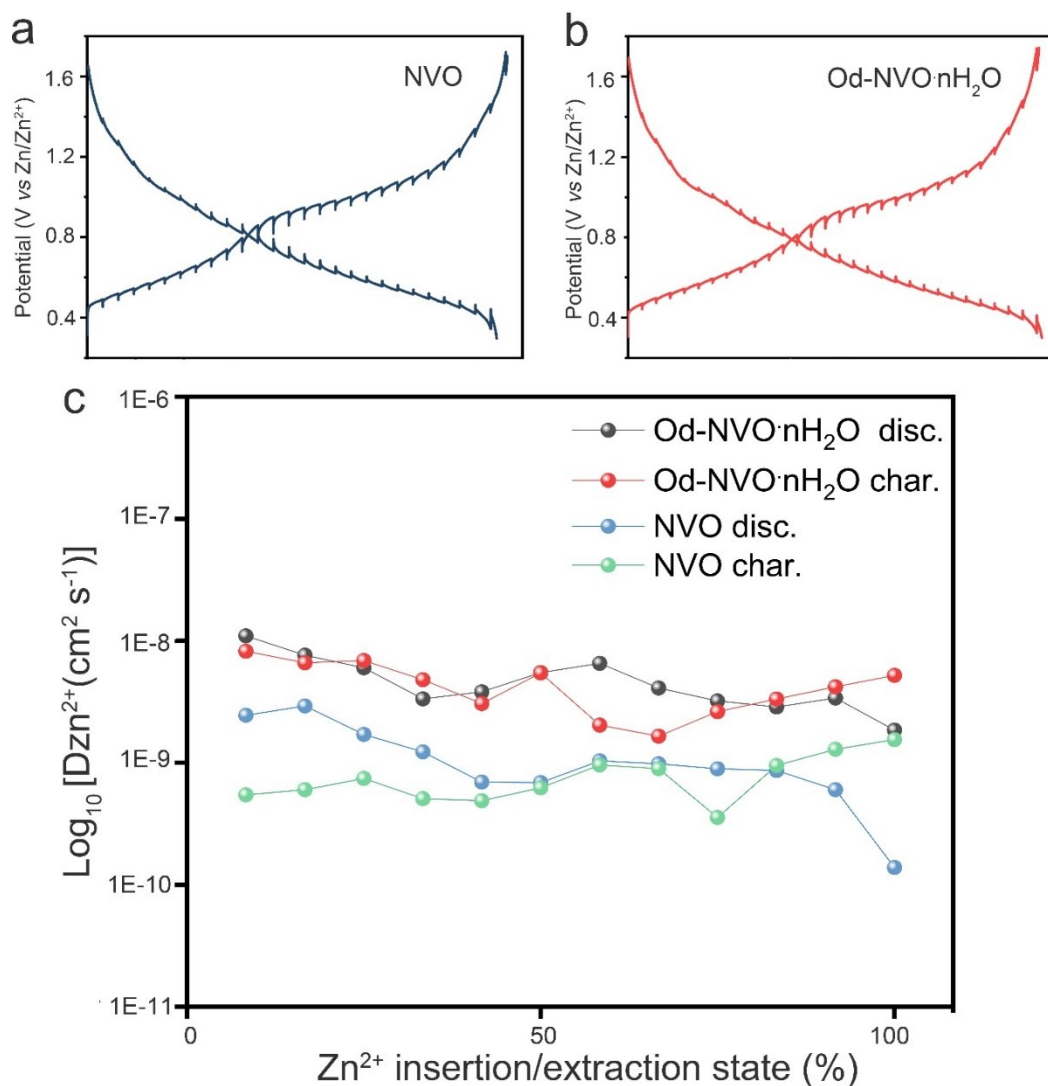
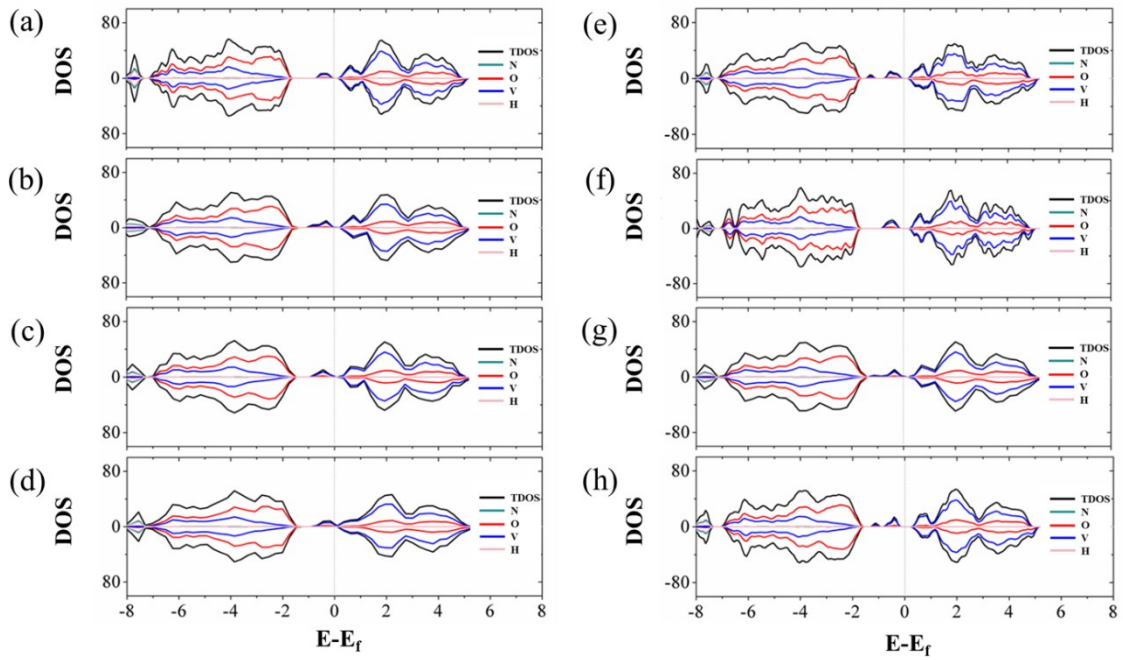
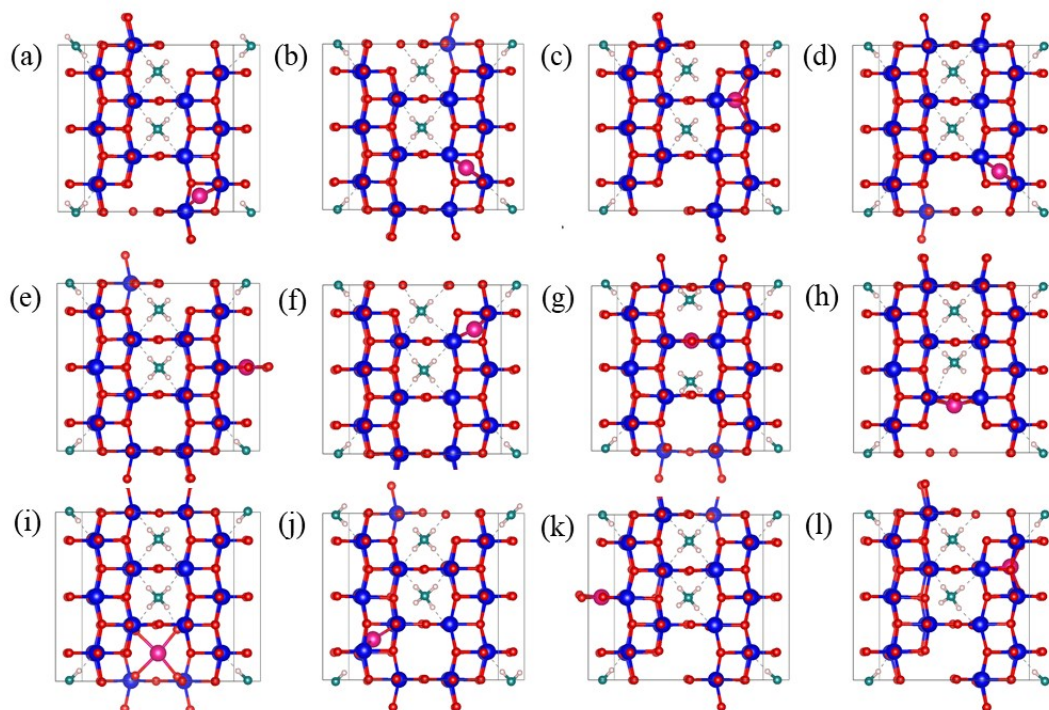


Figure S12. a,b) Charge–discharge GITT curves of as-fabricated cell using NVO and O<sub>d</sub>-NVO·nH<sub>2</sub>O as cathodes at a current density of 50 mA g<sup>-1</sup> and (c) the corresponding Zn<sup>2+</sup> diffusion coefficients as a function of Zn<sup>2+</sup> composition during the charge–discharge scan.



**Figure S13.** The projected density of states (PDOS) and the total density of states (TDOS) of (a) perfect NVO and NVO with oxygen point vacancy of (b) O1, (c) O2, (d) O3, (e) O4, (f) O5, (g) O6, and (h) O7. The dotted lines denote the Fermi levels.



**Figure. S14.** The insertion sites in (a)-(i) are the inequivalent insertion sites of Zn ion in perfect-NVO, in which the most stable and metastable insertion sites are (e) and (f). The insertion site near the oxygen vacancy is (j). The most stable and metastable insertion sites in defective-NVO are (k) and (l). The blue, red, green, fuchsia and light pink spheres represent V, O, N, Zn, and H, respectively.

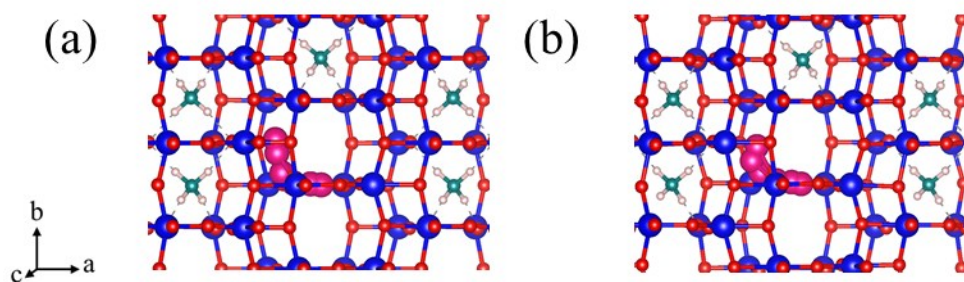


**Figure S15.** The diffusion pathways viewed along 001 orientation in (a) perfect-NVO and (b) defective-NVO. The blue, red, green, fuchsia and light pink spheres represent V, O, N, Zn, and H, respectively.

## Reference

- 1 Kresse, G.; Hafner, J. *Phys. Rev. B* 1993, **47**, 558.
- 2 Kresse, G.; Furthmüller, J. *Comput. Mater. Sci.* 1996, **6**, 15.
- 3 Perdew, J. P.; Burke, K.; Ernzerhof, M. *Phys. Rev. Lett.* 1996, **77**, 3865–3868.
- 4 Blöchl, P. E. *Phys. Rev. B* 1994, **50**, 17953.
- 5 Sarkar, T.; Kumar, P.; Bharadwaj, M. D.; Waghmare, U. *Phys. Chem. Chem. Phys.* 2016, **18**, 14, 9344–9348.
- 6 Klimeš, J.; Bowler, D. R.; Michaelides, A. *Phys. Rev. B* 2011, **83**, 195131.
- 7 P. He, G. Zhang, X. Liao, M. Yan, X. Xu, Q. An, J. Liu and L. Mai, *Adv. Energy Mater.*, 2018, **8**, 1–6.
- 8 C. Xia, J. Guo, P. Li, X. Zhang and H. N. Alshareef, *Angew. Chemie - Int. Ed.*, 2018, **57**, 3943–3948.
- 9 D. Kundu, B. D. Adams, V. Duffort, S. H. Vajargah and L. F. Nazar, *Nat. Energy*, 2016, **1**, 1–8.
- 10 P. Hu, T. Zhu, X. Wang, X. Wei, M. Yan, J. Li, W. Luo, W. Yang, W. Zhang, L. Zhou, Z. Zhou and L. Mai, *Nano Lett.*, 2018, **18**, 1758–1763.
- 11 B. Tang, G. Fang, J. Zhou, L. Wang, Y. Lei, C. Wang, T. Lin, Y. Tang and S. Liang, *Nano Energy*, 2018, **51**, 579–587.
- 12 B. Sambandam, V. Soundharajan, S. Kim, M. H. Alfaruqi, J. Jo, S. Kim, V. Mathew, Y. K. Sun and J. Kim, *J. Mater. Chem. A*, 2018, **6**, 3850–3856.
- 13 C. Xia, J. Guo, Y. Lei, H. Liang, C. Zhao and H. N. Alshareef, *Adv. Mater.*, 2018, **30**, 1–7.
- 14 J. Zhou, L. Shan, Z. Wu, X. Guo, G. Fang and S. Liang, *Chem. Commun.*, 2018, **54**, 4457–4460.
- 15 Q. Pang, C. Sun, Y. Yu, K. Zhao, Z. Zhang, P. M. Voyles, G. Chen, Y. Wei and X. Wang, *Adv. Energy Mater.*, 2018, **8**, 1–9.
- 16 J. Lee, J. Beck, W. Il, B. Won and S. Hyoung, *Electrochim. Acta*, 2013, **112**, 138–143.
- 17 W. Li, K. Wang, S. Cheng and K. Jiang, *Energy Storage Mater.*, 2018, **15**, 14–21.
- 18 G. Henkelman, B. P. Uberuaga and H. Jonsson, *J. Chem. Phys.* 2000, **113**, 9901.